Insight into the Process-Microstructure-Property Relationship: Single Splat Analysis, Adhesion Testing, and Thermal Cycling of Inner Diameter (ID) Thermal Barrier Coatings

Maheshwar Rao Bagathi
Forschungszentrum Jülich GmbH
Jonas Frederik Zajaczkowski
TU Dortmund University
Wolfgang Tillmann
TU Dortmund University
Daniel Emil Mack
Forschungszentrum Jülich GmbH
Robert Vaßen
Forschungszentrum Jülich GmbH
Georg Mauer
g.mauer@fz-juelich.de

Forschungszentrum Jülich GmbH https://orcid.org/0000-0002-0840-8006

Research Article

Keywords: Internal-diameter (ID), thermal-barrier coating systems (TBC), atmospheric plasma spraying (APS), splat morphology, coating adhesion, burner-rig cycling, isothermal oxidation, porous top coat, dense vertical cracked top coat (DVC), bond coat

Posted Date: December 2nd, 2025

DOI: https://doi.org/10.21203/rs.3.rs-8250483/v1

Additional Declarations: The authors declare no competing interests.

Insight into the Process-Microstructure-Property Relationship: Single Splat Analysis, Adhesion Testing, and Thermal Cycling of Inner Diameter (ID) Thermal Barrier Coatings

*Maheshwar Rao Bagathi [1], Jonas Frederik Zajaczkowski [2], Wolfgang Tillmann [2], Daniel Emil Mack [1], Robert Vaßen [1, 2], Georg Mauer [1, 3, *]*

[1] Forschungszentrum Jülich GmbH, Institute of Energy Materials and Devices, IMD-2: Materials Synthesis and Processing, 52425 Jülich, Germany

2 Ruhr University Bochum, Department of Mechanical Engineering, Institute for Materials, 44801 Bochum, Germany

[3] Institute of Materials Engineering, TU Dortmund University, 44227 Dortmund, Germany

** Corresponding author: g.mauer@fz-juelich.de*

Abstract

Although inner-diameter (ID) thermal barrier coating (TBC) processes are well-established for large aero/land-based turbine liners, the relationships between the processes, microstructures, and properties of coatings applied to smaller, highly confined passages (ID <200 mm), such as combustor liners, exhaust manifolds, and pipes that face comparable thermal loads, remain largely undocumented. This study examines 8 wt.% YSZ topcoats, which are deposited using an ID-atmospheric plasma spray (APS) torch, as well as bond coats, which are deposited using an ID-high velocity oxyfuel (HVOF) torch, inside 200 mm diameter, 8 mm wall tubes. The results are then compared with those of flat substrates sprayed under otherwise identical conditions. Single splats of YSZ demonstrate that oblique impact angles imposed by the tube create splashed lamellae, resulting in slightly higher local porosity than on flat substrates. Pull-off tests reveal the adhesion strengths of ID TBCs when sprayed using the two ID spraying systems. Two types of topcoat microstructures were developed using a lower-power ID-APS torch: porous variants with different porosities ranging from 9% to 17 vol% and a dense, vertically cracked (DVC) variant. The microstructures were subjected to (i) burner-rig thermal-gradient cycling and (ii) 1100 °C furnace cycling. In the burner rig, lifetime scales with the

through-thickness temperature gradient and bond-coat thickness. The best porous ID coating endured 246 cycles, while the specimen with a thin bond coat failed abruptly after 101 cycles. Furnace tests impose uniform oxidation; all porous coatings spalled between 60 and 100 cycles, and the DVC cracked after 40 cycles. The failure modes indicate, respectively, oxidation-driven delamination of the ceramic from the bond coat and cracking through the ceramic topcoat. In conclusion, disk-type splat formation, adequate bond coat thickness, and sufficient top coat porosity are microstructural prerequisites for durable ID-TBCs, providing a process map for future ID applications.

Keywords

Internal-diameter (ID); thermal-barrier coating systems (TBC); atmospheric plasma spraying (APS), splat morphology; coating adhesion; burner-rig cycling; isothermal oxidation; porous top coat, dense vertical cracked top coat (DVC); bond coat

Introduction

Thermal barrier coatings (TBCs) are widely used in high-temperature applications, such as aerospace engines, gas turbines, and automotive components, to protect the underlying metallic substrates from extreme heat exposure and environmental damage [1]. A typical TBC system consists of a metallic bond coat (for oxidation resistance) and a ceramic top coat (commonly 8 wt.% yttria-stabilized zirconia, 8YSZ). A thermally grown oxide (TGO) forms at the interface of the two layers during operation [2]. TBCs are predominantly applied to the external exposed surfaces of turbine blades, vanes, and combustors [1]. However, the internal surfaces of components such as pipelines, exhaust manifolds, and combustor liners also experience severe heat and could also benefit from TBC protection [3–5]. Coating these internal diameter (ID) surfaces is increasingly important for advanced component designs [6], yet this area is understudied due to the additional challenges involved [7–11]. Atmospheric plasma spraying (APS) is one of the most common methods for applying ceramic TBC top coats [12]. Conventional porous APS coatings (typically 10–20% porosity) have lower thermal conductivity and accommodate strain via distributed microcracks and inter-splat pores [1].

The primary design requirement of APS TBCs is a ceramic layer with high thermal shock resistance [13]. The performance and failure mechanisms of TBCs are closely related to their microstructure and the thermomechanical stresses that develop during operation. A common failure mode is spallation of the ceramic top coat, which is caused by progressive TGO growth at the bond coat interface [14]. As the TGO thickens during exposure to high-temperatures, it generates increasing stresses. Upon thermal cycling, these TGO-induced stresses, combined with mismatches in thermal expansion, can lead to interfacial cracking and eventual coating delamination [1]. Thus, a key design principle is managing TGO growth and relieving stress to extend TBC life [15]. One approach is to pre-oxidize the bond coat, forming a thin, uniform α-Al_2O_3 scale before depositing the top coat. This slows the subsequent TGO growth during service, delaying the onset of critical stress and significantly improving thermal cycling lifetime [16]. Another approach is the engineering of the top coat's microstructure. Dense vertically cracked coatings, for instance, introduce segmented crack networks that allow the coating to tolerate thermal strain without catastrophic damage [13]. Segmented APS coatings with high vertical crack density have been shown to possess greater in-plane compliance and longer spallation life under cyclic heating [17, 18]. In addition to standard furnace cycling, advanced thermal gradient cycling tests (burner-rig tests) are often employed to evaluate the lifetimes of these TBCs [15]. Burner-rig testing involves rapid heating and cooling the TBC specimens with a high surface heat flux to evaluate TBC durability. Early studies by Traeger et al. [19], for example, established burner-rig methods for testing TBC systems. These methods have since become a crucial tool for benchmarking new TBC architectures and materials.

Despite extensive research on TBCs for external surfaces, applying TBCs to the inner surfaces of small-diameter components remains a technological challenge. Coatings on inner surfaces (ID coatings) are rarely reported, and specialized techniques that address this need have only recently begun to emerge [8]. The internal diameter APS (ID-APS) process was developed to coat tubes and other confined geometries that traditional "line-of-sight" APS cannot adequately cover [10]. Apart from limited spray distance, several other unique challenges arise in ID-APS coatings. Heat accumulation and oxidation due to overheating of the substrate cause lower splat bonding strength [20]. Additionally, overspray and rebounding particles cannot easily dissipate in a tube; therefore, they tend to redeposit onto the surface, which increases the coating's porosity and compromises adhesion [21]. These issues complicate the coating formation in IDs compared to flat-surfaces. Recent work has only begun to address these problems. We recently reported successful APS deposition of YSZ TBCs inside small tubular components using a

specialized ID torch in combination with an HVOF-applied bond coat [22]. We found that achieving the desired porosity and microstructure on ID surfaces required careful adjustment of spray parameters (e.g., reduced plasma power and increased spray distance) and appropriate feedstock selection due to the limited space for plume development. These studies highlight the feasibility of ID coatings, but they also underscore our limited understanding of process–microstructure–property relationships in this new context.

The objectives of this study are to investigate the influence of the ID-APS process on the formation, microstructure, and performance of 8YSZ TBC coatings and to compare some characteristics with those of APS coatings on flat substrates. The study focused on two basic topcoat architectures: a porous microstructure and a dense, vertically cracked microstructure. These microstructures were deposited on the inner surface of tubular specimens. Because plasma-sprayed ceramic coatings are built splat-by-splat, the behavior of each individual lamella is foundational to the overall coating structure. Consequently, analyses of single-splat formation have demonstrated that coating performance is critically governed by the spreading and solidification behavior of individual molten droplets. Sampath et al. systematically varied the substrate temperature and demonstrated a sharp transition from fragmented "splash" splats to contiguous, disk-like lamellae once the surface temperature exceeded a critical range (approximately 150–300 °C for YSZ) [23]. Chandra et al. later generalized their findings by linking splat shape to the dimensionless Weber and Reynolds numbers. They emphasized the roles of particle enthalpy, viscosity, and substrate roughness [24]. More recently, Tillmann et al. investigated how arc current, substrate preheat, and gun angle influence the proportion of fully molten disks in an APS plume. They provided process maps that illustrate the splash-to-disk transition [25]. Crucially, Mutter et al. [26] correlated those splat statistics with bulk properties, showing that coatings dominated by disk-type lamellae exhibit lower porosity, a higher elastic modulus and a more benign residual stress state than coatings assembled from splash-type splats. These results highlight the importance of controlling splat formation through particle heating and substrate conditions to tailor coating microstructure. In an ID spraying scenario, differences in particle trajectories, impact angles, and substrate heat flux could significantly alter splat flattening and solidification compared to standard APS. This could lead to different microstructural outcomes. Therefore, examining splat morphology and deposition behavior under actual ID-APS conditions is essential for establishing a process-microstructure relationship.

First, single-splat experiments were performed on both ID and flat substrates to reveal how individual droplets spread and solidify under ID-APS conditions, as well as how this process governs coating buildup. Then, we measured the pull-off adhesion strength of the ID TBCs alongside the benchmarks for flat coatings. Finally, we performed thermal cycling tests to evaluate the lifetime of porous and DVC ID-TBCs relative to their counterparts on flat substrates. This comprehensive approach aimed to improve understanding of the relationships between the ID-deposited TBCs' process, microstructure, and properties. This knowledge should bridge the current technological gap and guide the development of robust TBCs for internal surface applications where conventional coating strategies are insufficient.

Materials and methods

Feedstock and substrate preparation

Bond coat

The bond coat feedstock was a gas-atomized CoNiCrAlY alloy powder (Praxair Co-210-6, with a nominal composition of 32% Co, 21% Ni, 8% Cr, 0.5% Y, and 5% Al by weight) with a particle size range of –22 to +5 µm. Gas atomization produces predominantly spherical to near-spherical particles with smooth surfaces and occasional satellites, promoting stable feeding and uniform heating in the high-velocity flame. While scanning electron microscopy (SEM) analysis confirmed the expected morphology and particle size distribution by volume, as measured by laser diffraction, matched the specifications given by the supplier, laser diffraction measurements by number gave a median diameter in the low tens of micrometers, with a d_{50} of about 3.8 µm and a d_{10} of less than 1.8 µm. This shift toward finer particles increases the surface area-to-volume ratio, which can result in low dynamic flowability, powder spitting, or enhanced nozzle clogging.

To counteract these effects, the powder was conditioned prior to spraying. A nanoscale fumed silica (SiO_2) flow-control agent (AEROSIL® 972, with a primary particle size of 50 nm) was added at a controlled mass fraction of 0.5 wt.% to serve as a rheological additive. The mixture was then placed in a tumble mixer for 60 minutes to allow the silica to adhere to the alloy particle surfaces and form homogeneous, nanometer-scale coverage. This coverage acted as a spacer between the CoNiCrAlY particles, limiting mechanical interlocking and reducing the

cohesive strength of the agglomerates. These modifications led to measurable improvements in mass-flow stability when feeding through the volumetric powder-disc system. Feed interruptions were reduced, and spray process reproducibility improved.

Top coat

Two 8 wt.% yttria-stabilized zirconia (8YSZ) ceramic powders were used for the thermal barrier top coats to create different microstructures, (1) an agglomerated and sintered (A&S) YSZ powder (HC Starck AMPERIT 827.006), which has a median particle size of d_{50} = 72 µm (particle size range: −125 to +45 µm), and (2) a coarse feedstock. This coarse feedstock was selected to produce a highly porous coating microstructure. (2) A fused-crushed YSZ powder (Oerlikon Metco Amdry 6643) with a median particle size of d_{50} = 29 µm and a particle size distribution (PSD) range of –45+11 µm was used to deposit dense, vertically cracked (DVC) coatings. The particle size and morphology of Amdry 6643 favor dense lamellae and vertical segmentation cracks [27, 28], yielding a strain-tolerant "DVC" microstructure in the topcoat. Both YSZ powders were partially stabilized zirconia (8 wt.% Y_2O_3).

Substrates

Three types of substrates were prepared for the experiments. For internal coating deposition, tubular stainless steel substrates (AISI 321H, X10CrNiTi18-10) with a 200 mm internal diameter were used to represent the inner diameter (ID) surfaces of small combustor cans and the exhaust system. For single splat investigations, the inner surfaces of the tubular substrates were machined using a lathe for boring and grinding, followed by polishing to a 2500-grit finish (approximately 6 µm R_a). Additionally, flat substrates (316L stainless steel plates measuring 30×30×3 mm) were mirror polished for comparative studies of splat morphology. Disc-shaped 316L stainless steel coupons (40 mm in diameter and 3 mm thick) were used for adhesion testing.

Prior to depositing the top coat, the bond-coated tubular substrates were placed in a tube furnace and heat-treated in a high-purity argon atmosphere (0.1 MPa) following a two-step schedule: 1120°C for two hours, then 845°C for 24 hours. The furnace was then opened and the substrates were cooled in air.

Coating Deposition

Bond coat deposition (ID-HVOF)

The CoNiCrAlY bond coat was applied using an ID-RED (Thermico Engineering GmbH, Dortmund, Germany) internal-diameter high-velocity oxy-fuel (ID-HVOF) spraying gun (Figure 1). The system consists of a compact combustion chamber with an 85° diverter that achieves ID coating. The torch was inserted coaxially into the cylindrical substrate. Coating was applied through the combined movement of axial translation of the torch and rotation of the workpiece. This ensured full circumferential coverage with uniform pass overlap.

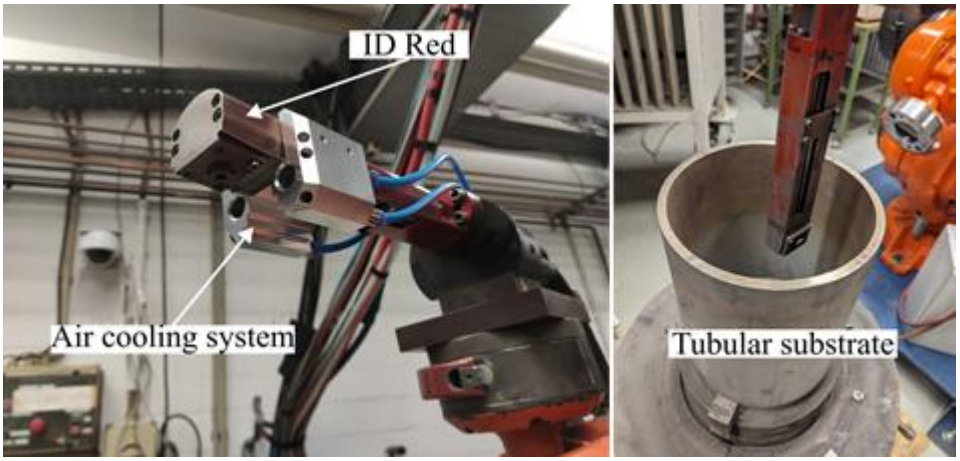

Figure 1. ID-HVOF setup for BC deposition on an ID-tubular substrate, left: ID Red ID HVOF torch with mounted air-cooling system; right: ID Red positioned inside of tubular substrate

To control the heating of the substrate in the confined geometry, cooling air was directed into the spray zone through an annular nozzle surrounding the torch barrel. Intermittent dwell periods were also programmed between spray passes. Spraying was carried out using process parameters that were previously optimized for low-porosity deposition (Table 1). The stand-off distance was set to 40 mm, the oxygen flow to 150 slpm, the hydrogen flow to 50 slpm, the kerosene feed to 3 l/h, and the carrier gas (N_2) to 10 slpm. These parameters were kept constant for all bond coat specimens in this study. Ten passes were carried out to achieve a target coating thickness of 130 µm. Afterwards, the surface roughness of the coated samples was measured using a tactile roughness and contour measurement system.

Table 1. High velocity oxyfuel spraying parameters for CoNiCrAlY bond coat an ID-HVOF torch ID Red.

HVOF process parameters	CoNiCrAlY bond coat
Kerosene flow	3 l/h
Hydrogen flow	50 slpm
Oxygen flow	150 slpm
Carrier gas flow	10 slpm
Meander width	2 mm
Substrate rotation	48 rpm
Robot speed	1.6 mm/s
Spray angle	85°
Powder feed rate	20 g/min
Spray distance	40 mm
Cooling air	0.6 MPa
Passes	10

slpm: standard liters per minute

Top coat deposition (ID-APS)

The ceramic topcoat was deposited using an atmospheric plasma spraying (APS) Multicoat facility (Oerlikon Metco, Wohlen, Switzerland), which was equipped with an SM-F100 CONNEX ID plasma torch. The torch had an 8 mm nozzle diameter and was mounted on a six-axis robot at the Jülich Thermal Spray Center (JTSC) in Germany. Figure 2 shows the ID-APS setup for the topcoat deposition on the ID-tubular substrates. Controlling the environment inside the tubular substrate also helps prevent overspray redeposition. In our setup, masking beyond the desired coating zone prevented the buildup of loosely attached particles on the ID surface, which can occur in closed cylinders. Process settings for the porous coatings followed the ID-APS parameters established in [22]. The four parameter sets selected for porous top coats in the present study are given in

Table 2. The arc current and spray distance were each set to a high and a low level. An integrated torch cooling system that used compressed air was available and was used as necessary to manage the substrate temperature during deposition.

The dense, vertically cracked (DVC) microstructure coatings were produced by making targeted adjustments to the variables governing columnar crack development, principally torch power, spray distance, high feed rate, and substrate temperature. Substrates were preheated using the plasma flame without powder feed prior to deposition to ensure consistent initial conditions. We deliberately kept integrated front cooling of the torch off to facilitate hotter conditions during deposition of the DVC-type coating. The corresponding plasma parameters are listed in

Table 2.

Figure 2. ID-APS setup for TBC deposition on ID-tubular substrate, left: F100 ID-APS torch placement in the 200-mm-diameter steel tube mounted on a turntable, center: in-flight photograph showing the plasma plume impinging on the rotating tube wall at a spray distance, of 120 mm, right: view after deposition showing the YSZ top coat on the full internal circumference; beyond the defined coating area the tube was masked to avoid overspray.

Table 2. Atmospheric plasma spraying parameters for YSZ-based coatings by CONNEX F-100. torch.

APS process parameters	Porous top coat	Dense vertically cracked (DVC) top coat
Current	330-380 A	350 A
Hydrogen flow	3-5 slpm	4 slpm
Argon flow	30 slpm	30 slpm
Carrier gas flow	2.5 slpm	2.5 slpm
Meander width	2 mm	2 mm
Substrate rotation	48 rpm	30 rpm
Robot speed	1.6 mm/s	1.6 mm/s
Spray angle	90°	90°
Powder feed rate	23 g/min	30 g/min
Spray distance	70-120 mm	60 mm

slpm: standard liters per minute

Single splat investigations

To clarify how individual lamellae contribute to coating build-up, single-splat experiments were conducted under each set of spray parameters. For inner-diameter tubular substrates, a custom masking fixture restricted the particle flux, allowing only a few molten particles to reach the tubular wall and preventing splat overlap. For comparison, mirror-polished stainless steel coupons (30×30×2 mm) were prepared and sprayed under identical conditions. Each substrate was preheated to the temperature recorded at the start of spraying for the corresponding parameter set (Table 2). Two conditions were investigated: a high-current setting (Set 1, 380 A) and a low-current setting (Set 2, 330 A). All other variables, including spray distance, hydrogen flow, and feedstock median size (d_{50} = 72 μm), were held constant to isolate the effect of arc current. The torch traversed the surface once at high speed to ensure that only

a few particles would impact the target. After spraying, the specimens were mounted and examined using a Hitachi TM3000 tabletop scanning electron microscope (SEM) (Hitachi High-Technologies Europe, Krefeld, Germany) to obtain high-magnification images of the resulting splats. For each spray condition, a single, well-isolated splat was selected. Two orthogonal chord lengths, D_1 and D_2, were measured across the widest part of the lamella using the calibrated SEM scale. The splat diameter was defined as the arithmetic mean to smooth any slight ellipticity in the footprint. Then, the flattening ratio was calculated as the ratio of the splat diameter to the d_{50} of the feedstock (D/d_{50}), where d_{50} = 72 µm, the median particle size of the feedstock, as measured by laser diffraction.

Adhesion tests

Adhesion strength was determined using a pull-off test according to the procedure defined in DIN EN 582 (Figure 3). Circular test coupons (40 mm in diameter) were manufactured from AISI 316L stainless steel. AISI 321H stainless steel was used for the substrates in the other property evaluations; however, discs in this grade were unavailable at the time of testing. Due to its comparable mechanical properties, thermal expansion coefficient, and chemical composition, AISI 316L was selected as a substitute to ensure that differences in adhesion performance could not be attributed to substrate material effects. The coupons were coated with a CoNiCrAlY bond coat, which was deposited by internal-diameter HVOF using previously established, optimized, low-porosity parameters. Two porous YSZ topcoats were applied to three samples each for two spray distances, resulting in distinct porosity levels (Table 3).

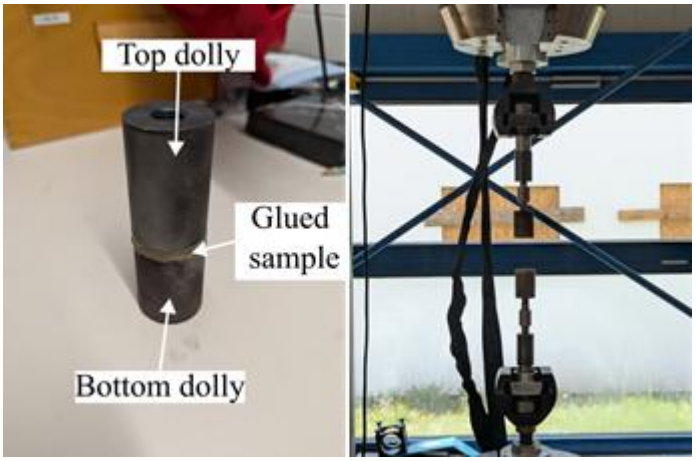

Figure 3. Left: sample setup for adhesion testing; right: sample mounted in universal testing machine after testing.

Table 3. Operating parameters used for the internal-diameter atmospheric plasma-spray (ID-APS) single-splat experiments.

ID-APS process parameter	Set 1	Set 2
Spray distance	120 mm	120 mm
Arc current	380 A	330 A
H_2 flow rate	5 slpm	5 slpm
Feed-stock median size, d_{50}	72 µm	72 µm

slpm: standard liters per minute

For testing purposes, the coated surfaces were bonded to grit-blasted steel loading fixtures (dollies) with a R_z of 40 µm using a high-strength polymer adhesive (FM 1000, with a cure temperature of 180°C). The adhesive was applied as a 0.25-mm-thick foil. During curing, a constant force of 10 N was applied. Tests were conducted on a universal testing machine equipped with a tensile alignment fixture to ensure axial load application. The load was applied at a force of 1 mm/min until the coating detached. The maximum load at failure was recorded and converted to adhesion strength by dividing it by the bonded area. After testing, the fracture surfaces were examined using optical microscopy to identify the location and mode of failure.

Thermal cycling tests

Each sample identified by a "BRT" or "FCT" code, corresponds to one of four APS parameter sets applied to 200-mm-ID steel tubes. After coating, burner-rig specimens (BRT-1 to 4) and furnace-cycle samples (FCT-1 to 5) were cut from the same tubular substrates. Table 4 provides the spray distance, H_2 flow rate, and arc current for each set.

Table 4. APS spray parameters for 8YSZ topcoat deposition inside 200 mm ID tubes; burner-rig specimens (BRT-1 to 4) and furnace-cycle coupons (FCT-1 to 5) were sectioned from these coated tubes.

Burner rig cycling test	Furnace cycling test	APS process parameters		
Sample	Sample	Spray distance (mm)	Hydrogen flow (slpm)	Current (A)
BRT-1	FCT-1	120 mm	5 slpm	330 A
BRT-2	FCT-2	70 mm	3 slpm	330 A
BRT-3	FCT-3	120 mm	5 slpm	380 A
BRT-4	FCT-4	70 mm	5 slpm	380 A
-	FCT-5 (DVC)	70 mm	4 slpm	350 A

slpm: standard liters per minute

Burner rig tests

The thermal cycling behavior of the coating systems was tested using a thermal gradient test rig [19]. It was used to subject ID-TBCs to repeated thermal cycles. The rig layout is illustrated in Figure 4. For the tests, rectangular coupons (100 × 100 mm) were cut from the ID-coated, 200-mm-diameter tubular substrates. The coupons were mounted with the concave side facing the flame in a stainless-steel support frame. The frame constrained the coupon along its perimeter, leaving a free surface for optical access. The TBC-coated specimens were subjected

to direct flame heating on the ceramic surface, and the metal substrate was cooled concurrently by compressed air from the backside. This produced a severe through-thickness temperature gradient. To eliminate edge effects and create a localized heating zone, the CH_4 burner nozzle was placed at the geometric center of the coupon (Figure 4). At the chosen spray distance, the hot core impinged on a circular spot with a diameter of 7-8 mm; the surrounding area remained cooler. This ensured that spallation initiated only within the highly stressed zone, while the edges provided mechanical restraint. The coating surface temperature is monitored at the hot spot with a pyrometer, and the substrate temperature is measured with a thermocouple fixed to a drilled hole close to the bond coat/substrate interface in the middle of the substrate. The emissivity of the coating surface was set to unity in the pyrometer settings, which is close to what can be expected. However, no reliable emissivity values are available. According to this assumption, the temperature is slightly underestimated by 40-50 K for YSZ, a factor that must be considered. However, the comparability between different measurements is unaffected.

One thermal cycle consisted of (i) heating the coupon for 5 minutes to a surface temperature of 1320 ± 20°C, followed by (ii) forced-air cooling of the front side of the coupon for 5 minutes so that a surface temperature of approximately 100°C was reached. During the first five cycles, the flows of the burner gas and cooling air were adjusted to achieve a temperature drop of 400 K between the sample's surface and the substrate. These flow settings were maintained throughout the entire test until coating failure. Assuming that heat flow does not change significantly during testing, changes in measured temperatures indicate structural changes in the coating (e.g., cracks or spallation). Coating failure was defined as the appearance of macroscopic spalls or through-cracks in the ceramic topcoat. All failed samples were cross-sectioned for post-test characterization using a Hitachi TM3000 tabletop SEM (Hitachi High-Technologies Europe, Krefeld, Germany) to identify microstructural features.

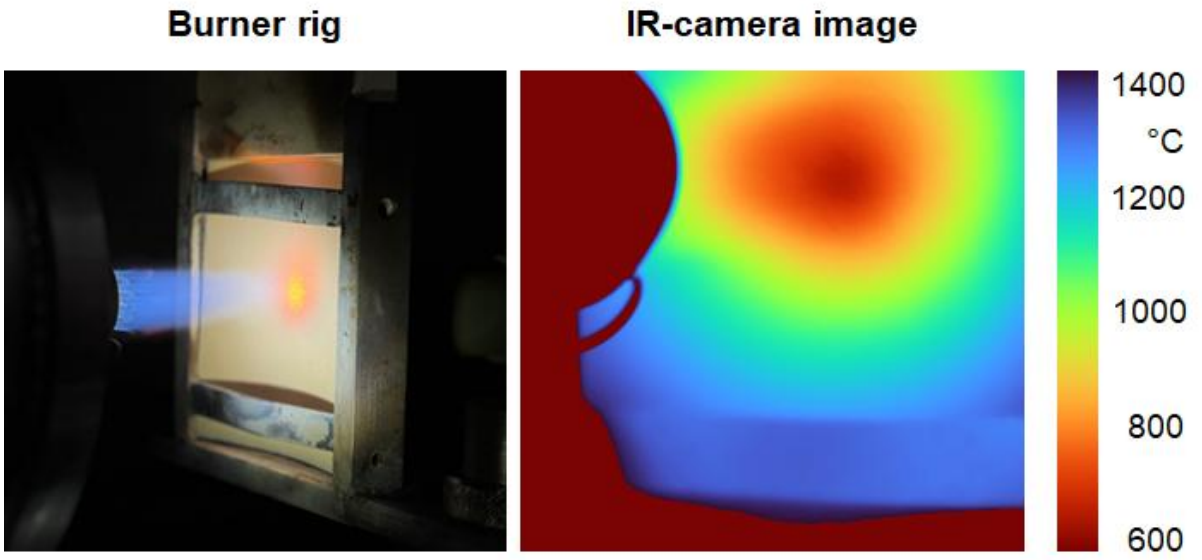

Figure 4. Methane flame impinging on the 7–8 mm heated spot of the YSZ coating.

Isothermal furnace tests

The TBC performance under isothermal conditions was evaluated by furnace cycling. Coated samples (50×50 mm square coupons cut from coated tubes) were placed in a preheated box furnace at 1100 °C for a two-hour dwell period. The samples were then cooled for 15 minutes. This heating and cooling cycle was repeated until failure. This was defined as the number of cycles at which more than 20% of the ceramic topcoat spalled off, exposing the bond coat.

Results and discussion

Single splat analysis

Figure 5 summarizes the morphologies obtained when individual 8YSZ droplets impacted either the curved inner diameter (ID) tube or a polished flat substrate both of which were preheated to the same temperature recorded at the start of spraying for APS process parameter set 1 (120 mm spray distance, 380 A current, H_2 flow 5 slpm).

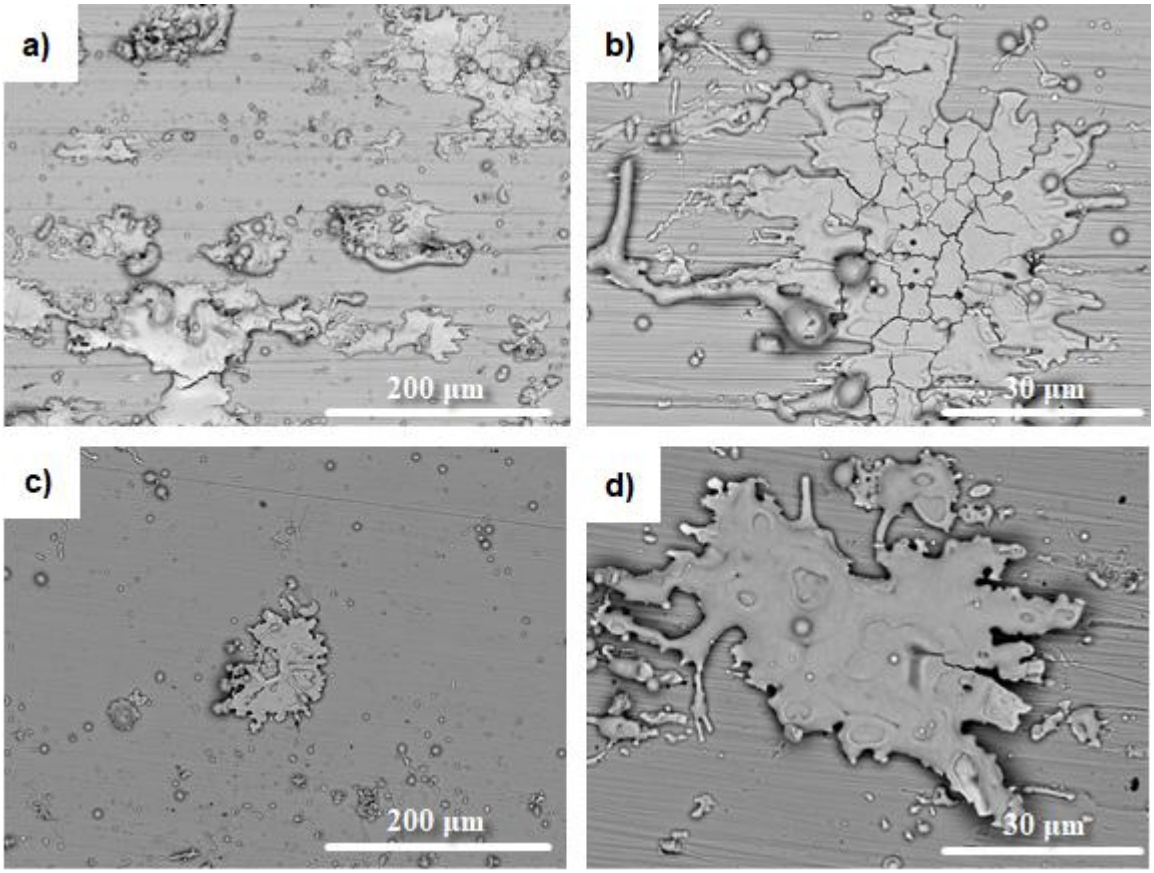

Figure 5. SEM micrographs of single 8YSZ splats deposited with parameter set 1 (380 A, 120 mm spray distance, 5 slpm H_2) on the inner tube wall *(a, b) and on a flat coupon (c, d*).

Figure 5 a) shows that, at low magnification, splats populate the ID surface as elongated, highly irregular islands aligned parallel to the tube's machining grooves. Figure 5 b) shows extensive "fingering" and micro-jetting at higher magnification. The individual fingers are 10–20 µm long and primarily extend along the surface grooves. This indicates that the tangential component of the droplet velocity vector is preserved on the curved surface. This behavior is characteristic of oblique impacts and/or reduced wetting on a rough surface, both of which promote splashing at the splat rim [29]. The central lamella exhibits a dense network of cracks (cell size 5–15 µm) that penetrate the entire lamella thickness. Such cracking is a signature of severe tensile stresses that arise when a splat solidifies while still at a temperature well above that of the massive 8-mm-thick tube wall. Such cracks are absent from splats on the thinner polished flat substrate in Figure 5 d). Apparently, the quenching rate in the solidifying splat is higher on a thicker substrate, which acts as a heat sink. The numerous circular blisters (1–3 µm) in the core region suggest that some unmolten inclusions were trapped beneath a rapidly

frozen crust. The equivalent diameter of 86 μm, with a feedstock median of 72 μm, yields a flattening ratio [30] of $D/d_{50} = 1.2$. This ratio indicates of enhanced lateral flow produced by the oblique incidence on a curved wall.

In Figure 5 c and d, only isolated splats are visible on the polished flat substrate. Their average equivalent splat diameter is 62 μm**,** which is roughly 30% smaller than the ID case. This difference is attributed to the normal impact on the planar surface and to the lower roughness ($Ra < 0.02$ μm), which limits interfacial friction. The periphery of the representative splat in Figure 5 d is compact and largely free of the long fingers seen on the ID surface. Only short lobes, 5–8 μm, long are present. The circular outline and absence of satellite droplets indicate excellent wetting and negligible rebounding. The smooth, crack-free interior of each lamella indicates that the 2-mm-thick, flat substrate cannot sustain the tensile stresses that develop in the coating on the thicker tube wall. It is hypothesized that the quenching rate is lower on this thinner flat substrate, resulting in fewer stresses built up during splat solidification and fewer cracks formed. The flattening ratio is $D/d_{50} = 0.9$, i.e., 25 % lower than that on the ID surface.

With the lower-current parameter set 2 (120 mm spray distance, 330 A current, 5 slpm H_2 flow), the curved ID tube receives far fewer large lamellae than the set 1. Instead, its surface is populated with satellites that are ≤ 5 μm and hemispherical indicating vigorous splashing (Figure 6 a, b). The splats yield an equivalent splat diameter of 65 μm, which corresponds to a flattening ratio of $D/d_{50} = 0.9$. This value is 25 % lower than for the set 1 on the same surface ($D/d_{50} = 1.2$), which confirms that reduced plasma power markedly curtails lateral flow. Each lamella is bounded by a ragged rim of fine jets and droplets aligned with the tube's machining grooves. This confirms hydrodynamic fingering, which is induced by the combined effects of oblique incidence and higher melt viscosity [30]. Internally, coarse cracks ranging from 10 to25 μm in width traverse the full thickness. Numerous 1–3 μm spherical blisters in the core indicate vapor entrapment beneath a crust that froze rapidly on the massive 8-mm wall.

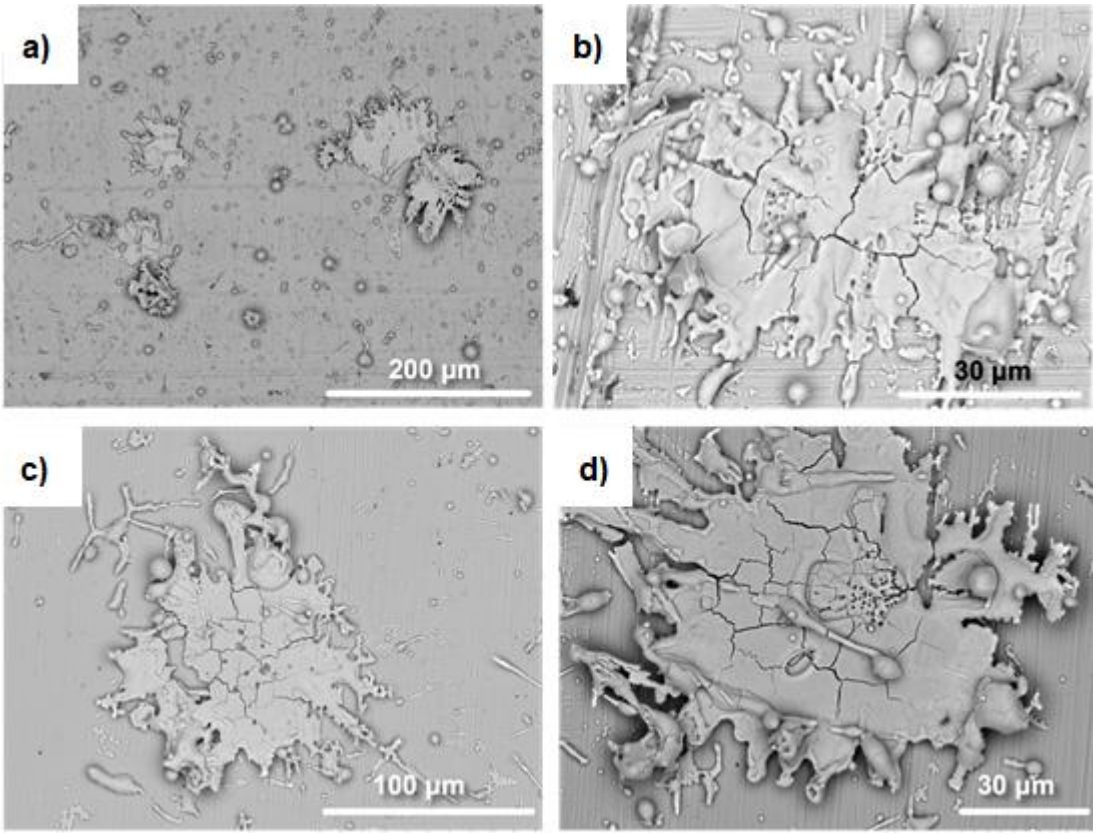

Figure 6. SEM micrographs of single 8YSZ splats deposited with parameter set 2 (330 A, 120 mm spray distance, 5 slpm H_2) on the inner tube wall *(a, b) and on a flat coupon (c, d*).

On the polished flat substrate (Figure 6 c and d) the same spray parameters generate isolated, but much larger lamellae surrounded by a micron-scale satellites which is typical of splash breakup when a partially molten droplet reaches the substrate. The representative splat diameter 110 µm, corresponding to $D/d_{50} = 1.5$, which is almost double the value on the ID surface. The greater spread could be the result of a normal impact and the absence of substrate surface effects (e.g., by roughness and groves). Some rim instabilities and long ligaments froze before full retraction. The central region of the splat exhibits a dense polygonal crack network with 15–30 µm cell spacing.

Implications for coating build-up

The single-splat experiments confirm that curvature primarily affects how the initial droplets spread, crack, and shed satellites. However, it has only a subtle impact on the final coating architecture. On the curved inner diameter (ID) wall, the spray strikes at an inherently oblique

angle, allowing the molten droplet to maintain significant tangential momentum. Instead of spreading uniformly in all directions, the melt is diverted around the tube wall in a circumferential manner. During normal impact, the radially symmetric outflow is replaced by a directional surge that produces elongated fingers following the direction of relative motion between the torch and the substrate. These features are attributed to higher tangential momentum and rapid peripheral solidification, which pinches off the rim rather than forming a concentric splash ring. This corresponds to a spreading mode as quantified for oblique impacts on inclined substrates by Kang et al. [29]. Eventually, the grooves affect the spreading direction as well. The ID splats at 330 A display pronounced fingering and abundant satellites (≈ 8–15 per splat), as well as irregular radial cracks. In contrast, those at 380 A still form disks, but have short rim lobes and tight ≈ 5–15 μm splat-crack cells.

On the polished, flat substrate, the higher-enthalpy (380 A) droplets flatten into near-circular disks with modest radial and concentric cracks, as well as a few satellites. In contrast, though the lower enthalpy (330 Å) droplets spread further than their ID counterparts, they are far from compact. Two to five satellites clinging to each splat indicate that reduced enthalpy can trigger rim instabilities and tensile cracking, even at normal incidence.

However, the fully built coatings produced on the inner tube wall and on the flat substrate exhibit only minor microstructural distinctions that are within the range of experimental scatter (0.5% to 0.9%) and statistically identical in porosity. The as-sprayed microstructures on the flat substrates were previously reported in [22] and are summarized for the curved substrates in Figure 3. This convergence suggests that the deposition process gradually reduces the geometric and cracking anomalies in the initial lamellae. Ultimately, both substrates assemble the same mesoscale architecture: interlocking 8YSZ lamellae separated by intersplat boundaries, despite the pronounced differences in their initial single-splat morphologies. Therefore, substrate curvature, local impact angle, and surface roughness jointly dictate initial lamella integrity but do not fundamentally alter the bulk APS coating architecture when process parameters are properly adjusted.

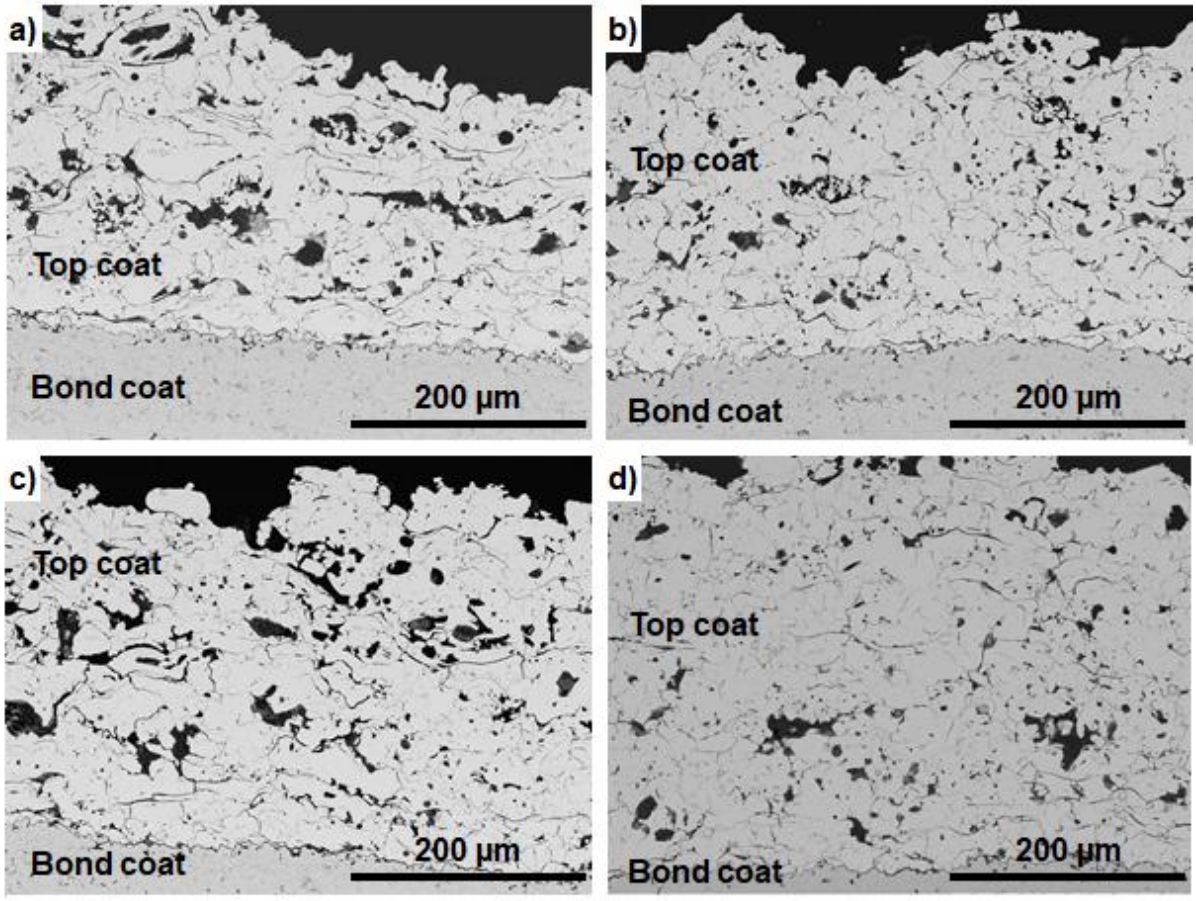

Figure 7. Cross-sectional SEM images of as-sprayed 8YSZ top coats deposited inside the 200-mm tube with identical feedstock and same number of passes, but different plasma parameters, (a) BRT-1: 70 mm spray distance, 330 A, 3 slpm H_2; porosity 17 vol %, thickness 279 µm, (b) BRT-2: 120 mm spray distance, 330 A, 5 slpm H_2; porosity 13 vol %, thickness 296µm, (c) BRT-3: 120 mm spray distance, 380 A, 5 slpm H_2; porosity 14 vol %, thickness 314 µm, (d) BRT-4: 70 mm spray distance, 380 A, 5 slpm H_2; porosity 9 vol %, thickness 466 µm.

Adhesion test results and analysis

The measured adhesion strengths ranged from 16.3 MPa to 35.0 MPa across all specimens. For the group with a 70-mm top coat stand-off distance, adhesion strengths were 21.0 MPa, 22.6 MPa, and 27.6 MPa, resulting in an average of 23.8 ± 3.4 MPa (n = 3). The group with 120 mm stand-off distance achieved adhesion strengths of 35.0 MPa, 22.0 MPa and 16.3 MPa, with an average of 24.4 ± 9.6 MPa (n = 3). No statistically significant difference was observed between the two stand-off groups was observed, indicating that the variation in top coat spray distance did not measurably affect adhesion under these conditions.

Fracture primarily occurred at the interface between the bond coat and the top coat in every specimen, with some samples exhibiting glue failure, see Figure 8. This consistent failure mode and the similar adhesion strengths across stand-off distances suggest that the relatively low surface roughness (R_a = 5.5 µm) of the optimized ID-HVOF bond coat was the primary limiting factor for adhesion, restricting mechanical interlocking with the APS ceramic layer.

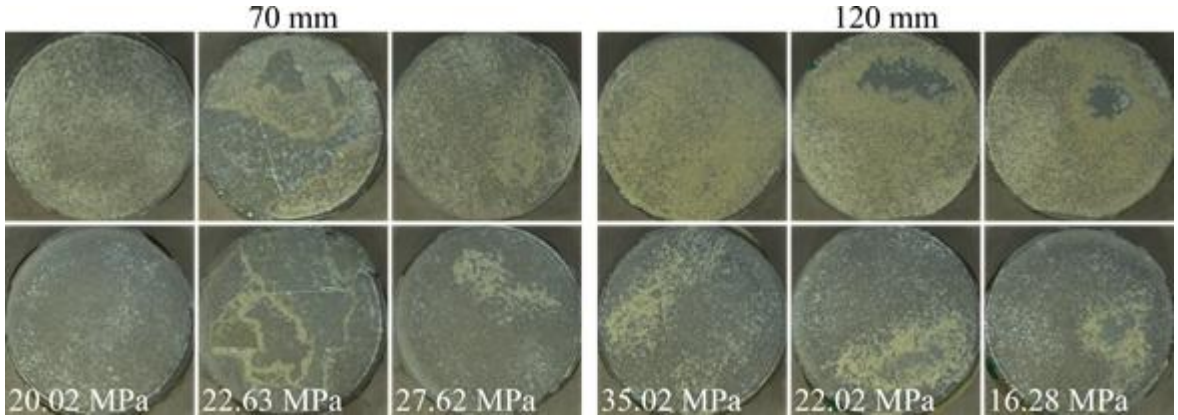

Figure 8. Fracture surfaces of adhesion test samples; top row: top dolly after pull-off tests; bottom row: coated sample surfaces after pull-off tests; dark areas indicate glue failure; yellow areas indicate failure at the BC-TC interface.

All tests were performed on 316L stainless steel coupons, which were chosen as an alternative to the 321H substrates used in other property evaluations. Because of their similar mechanical properties, chemical composition, thermal expansion coefficient, and failure mode at the bond coat-top coat interface, using 316L instead of 321H is not expected to affect the measured adhesion strength.

Thermal cycling behavior in the burner rig

Burner rig tests were performed on the four APS thermal barrier coatings on the inner surface of the 321H steel tubes (BRT-1 to 4, see Table 4).

Temperature-drop evolution

As mentioned earlier the temperature drop (ΔT) between the surface and the substrate was adjusted to 400 K during the first cycles when the burner rig tests began. Thereafter, ΔT exhibited a nearly linear relationship with cycling time for all samples indicating a steady loss of insulation efficiency over time. This gradual degradation is followed by an abrupt drop during the final few cycles. As shown in Figure 9, the surface–substrate temperature difference (ΔT) exhibits a steeper intermittent slope for BRT-1 and BRT-2, and a shallower slope for BRT-3 and BRT-4. This drift suggests subtle changes in the thermal barrier properties due to cracking, sintering [31], or TGO formation during exposure. However, small interfacial cracks do not immediately affect the temperature profile throughout the thickness [32, 33].

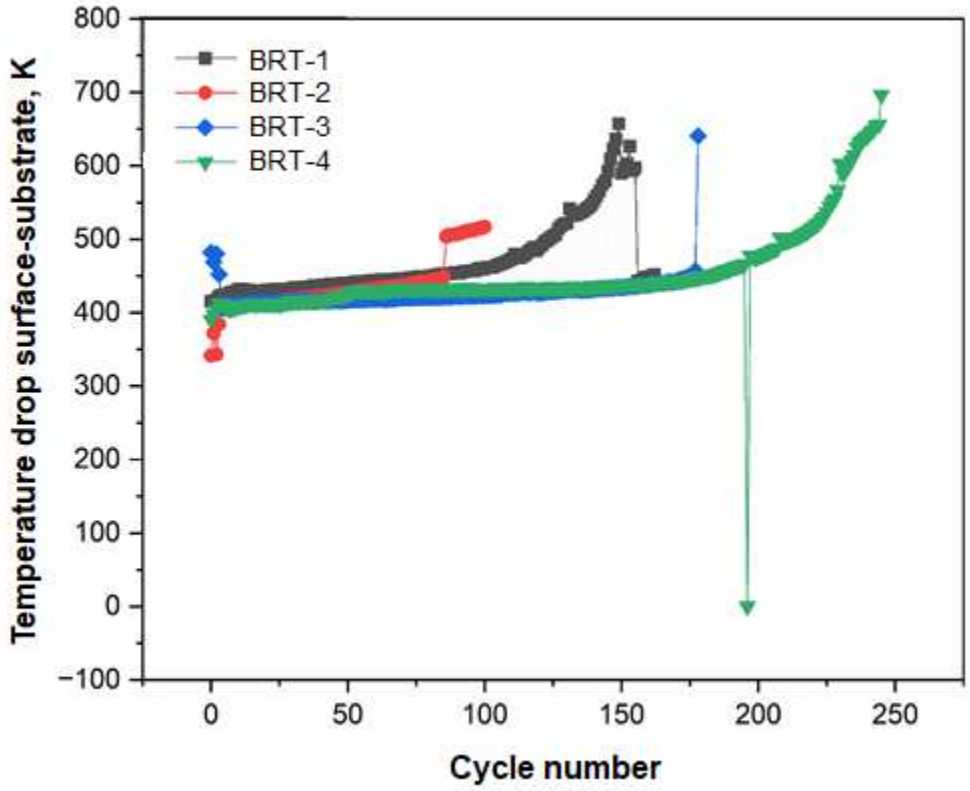

Figure 9. Temperature drop (ΔT) between surface and substrate during each heating segment of the burner-rig cycles.

As summarized in Table 5, lifetimes (cycles to failure) vary considerably depending on coating design. Failure was identified by a sudden increase of at least 50% in the temperature difference (ΔT) between the coating surface and the substrate. This increase in temperature is indicative of increased insulation as visible delamination of the topcoat marks the end of the coating's life. Using this criterion ensured that failure corresponded to substantial damage of the coating rather than minor cracking. Specifically, failure occurred at the following cycles: 101 for BRT-2, 163 for BRT-1, 179 for BRT-3, and 246 for BRT-4 (the longest lifetime). The best-performing coating (BRT-4) endured approximately twice as many cycles as the worst-performing coating (BRT-1). This highlights the significant impact of microstructural and architectural differences on TBC durability.

Table 5. Microstructural evolution and lifetime of ID-TBC samples after burner-rig cycling; the table lists the as-sprayed top coat porosity and thickness, bond coat thickness, the porosity remeasured after testing, the final α-Al_2O_3 TGO thickness, the aluminum depletion depth in the CoNiCrAlY, and the number of cycles sustained until failure.

Burner rig tests	As-sprayed properties			Burner rig tested coating properties			
Sample	As-sprayed topcoat porosity (Vol %)	As-sprayed topcoat thickness (µm)	Bond coat thickness (µm)	Burner rig tested topcoat porosity (Vol %)	TGO thickness (µm)	Depletion zone (µm)	No. of cycles
BRT-1	17%	279	132	15.7	0.5	6.8 ± 1.3	163
BRT-2	13%	296	100	11	0.5	7.9 ± 1.6	101
BRT-3	14%	314	145	11.8	0.9	11.8 ± 1.9	179
BRT-4	9%	466	141	8.2	0.5	7.4 ± 1	246

Influence of coating architecture and microstructure on thermal cycling life

Despite sharing the same substrate and similar testing conditions, the cyclic lives of the samples differed substantially (from 101 to 246 cycles). This variation is explained by differences in coating architecture and microstructure (Table 5) and is summarized graphically in Figure 10. The 8YSZ topcoats in this study differed in thickness and as-sprayed porosity due to varied plasma spray parameters (spray distance, torch current, and H_2 flow). These differences are clearly evident in porosity evolution (Figure 10 a) and life versus stand-off distance (Figure 10 b). It's evident that the samples sprayed with higher torch power (BRT-3 and BRT-4) and shorter spray distance (BRT-1 and BRT-4) have increased lifetimes. Notably, differences in bond coat thickness (Al reservoir), topcoat thickness (thermal gradient distribution), and APS spray parameters (porosity and splat bonding) had a significant impact on coating life and failure modes (Figure 10 c and d). It is conceivable that the samples sprayed under hotter condition with a higher torch power and a shorter spray distance had better deposition efficiency and, thus, better intersplat bonding.

Table 6. Thermal cycling parameters and lifetimes of the four ID-TBC substrates tested in the burner rig.

Sample	Topcoat thickness (µm)	Bond coat thickness (µm)	Logged surface T_{mean} ± SD (°C)	Logged substrate T_{mean} ± SD (°C)	Calculated bond coat T (°C)	Temp. gradient (K µm^{-1})	Cycles to failure
BRT-1	279	132	1337 ± 75	867 ± 77	1045	1.05	163
BRT-2	296	100	1287 ± 63	852 ± 68	1010	0.94	101
BRT-3	314	145	1274 ± 65	848 ± 78	998	0.88	179
BRT-4	466	141	1317 ± 72	863 ± 68	984	0.71	246

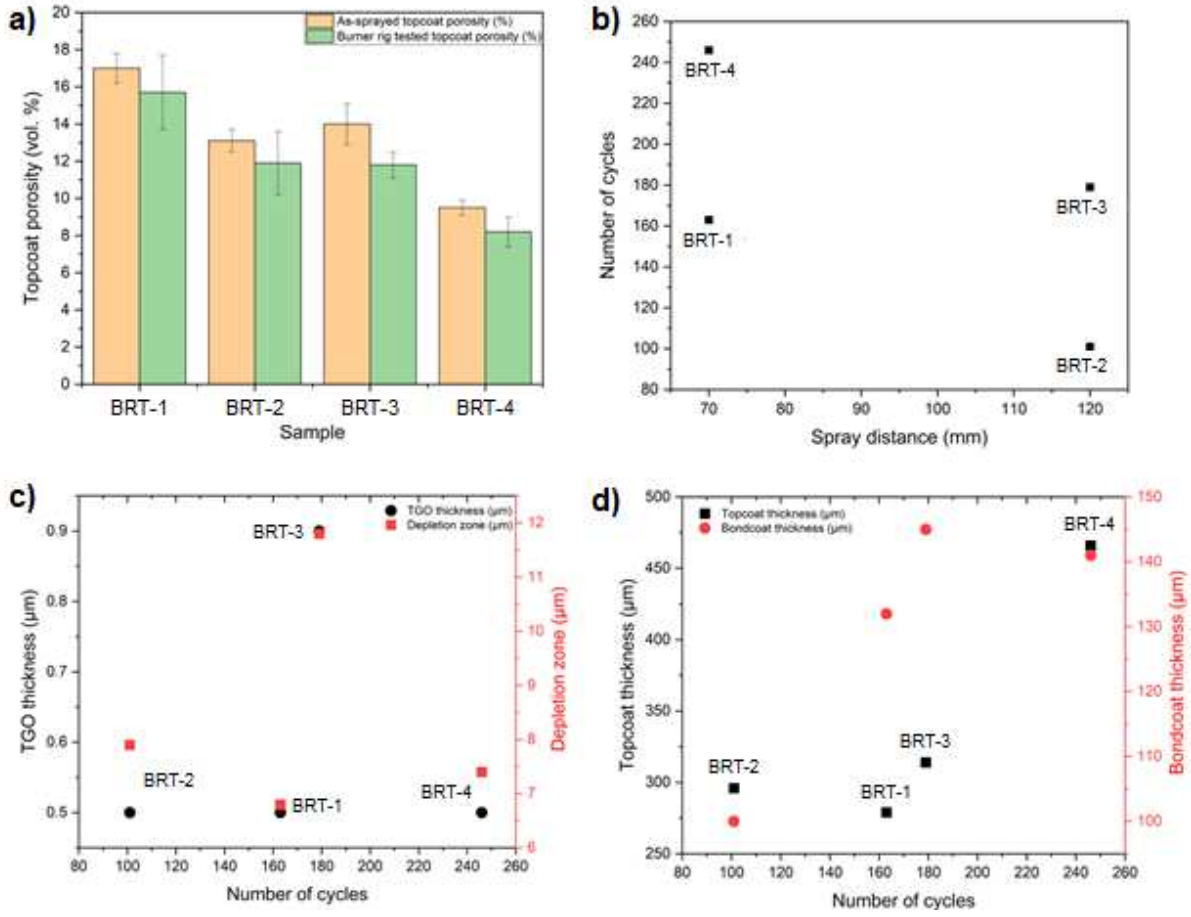

Figure 10. Parametric correlation between processing, microstructure and burner-rig life of the four ID-TBC coupons; (a) as-sprayed and post-test top-coat porosity; error bars denote the standard deviation of five image-analysis fields; (b) cycles to first spallation plotted against plasma-spray stand-off distance used for each coupon; (c) the relationship between life and interfacial oxidation: black points show final α-Al_2O_3 TGO thickness (left axis), red points the corresponding aluminum depletion depth in the bond-coat (right axis); (d) influence of coating architecture on life: black squares give top-coat thickness (left axis) and red circles the bond-coat thickness (right axis) versus cycles sustained.

All four coatings underwent measurable densification during burner-rig cycling (Figure 10 a). BRT-1 porosity decreased from 17 vol.% to 15.8 vol.%, BRT-2 from 13 to 11.8 vol.%, BRT-3 from 14 to 12 vol.%, and BRT-4 from 9.5 to 8.5 vol.%. This 1–2 vol.% reduction reflects the sintering of splats and the partial closure of intersplat pores. This raises the thermal conductivity and reduces the topcoat's compliance. Thus, a continuous increase in ΔT occurrs, as shown in Figure 9.

The interplay between bond coat thickness and topcoat characteristics can explain the observed lifetimes. BRT-4, with its thick bond coat and dense, thick topcoat, exhibited minimal sintering

(Figure 10 a) and the slowest TGO growth per cycle (only 0.5 µm during 246 cycles) (Figure 10 c). Its thick bond coat developed an Al-depleted zone of 7 µm, which is a small fraction of its 141 µm thickness, yet it still provides a large aluminum reservoir. BRT-2 (thin BC, moderate topcoat thickness) was essentially the opposite. Its 100 µm thick bond coat lost Al in an 8 µm layer after 101 cycles (nearly 8% of the bond coat thickness). Since the TGO was only 0.5 µm thick, the incipient aluminum depletion and possibly the formation of transient local oxides could have caused stresses at the interface. Combined with its higher bond coat temperature (due to a thinner ceramic), this led to crack initiation at comparatively fewer cycles. Additionally, BRT-2's moderate porosity (13%) did not provide as much strain relief as BRT-1 with an as-sprayed porosity of 17%. Yet, it densified appreciably during cycling, as shown in Figure 10 a. This combination of reduced compliance and increased sintering ultimately lowered durability.

BRT-3 (with a thick BC of 145 µm and moderate porosity) exhibited superior oxidation resistance and grew the largest TGO (0.9 µm; see Figure 10 c). Its life of 179 cycles, slightly higher than that of BRT-1, likely resulted from the effect of the bond coat thickness. However, BRT-3 did not reach the life of BRT-4. This is probably because its topcoat did not insulate as well or provide as much mechanical robustness as the 466 µm, 9% porosity topcoat of BRT-4.

Spallation modes and TGO characteristics

BRT-2 failed by a single, roughly 5 mm² patch (Figure 11a). In contrast, BRT-1 formed a larger central spall (several cm², Figure 12 c) and BRT-3 exhibited a narrow strip of coating loss (Figure 12 e). BRT-4 showed only minor chipping (Figure 12 a), which is consistent with its longest life. Cross-sectional SEM analysis revealed that all samples developed a continuous thermally grown oxide (TGO) layer at the TBC/bond coat interface. Despite the high surface temperatures, all samples formed a rather thin TGO (~0.5–0.9 µm of Al_2O_3) by the time of failure. This is far below the typical critical TGO thickness of 5–6 µm at which APS TBCs usually transition to TGO-driven spallation [32,33). Because the test conditions are not steady and the time at maximum temperature is only short, the oxide did not have time to grow thick under these rapid-cycle conditions. Most of the larger cracks are not observed at the TGO/ceramic interface, but rather, within the ceramic. This "gray" to "white" failure mode can be interpreted as resulting primarily from the high cyclic frequency and the gradient through

the thickness rather than from the relatively low stresses originating from the TGO growth. This shifts the crack plane into the ceramic.

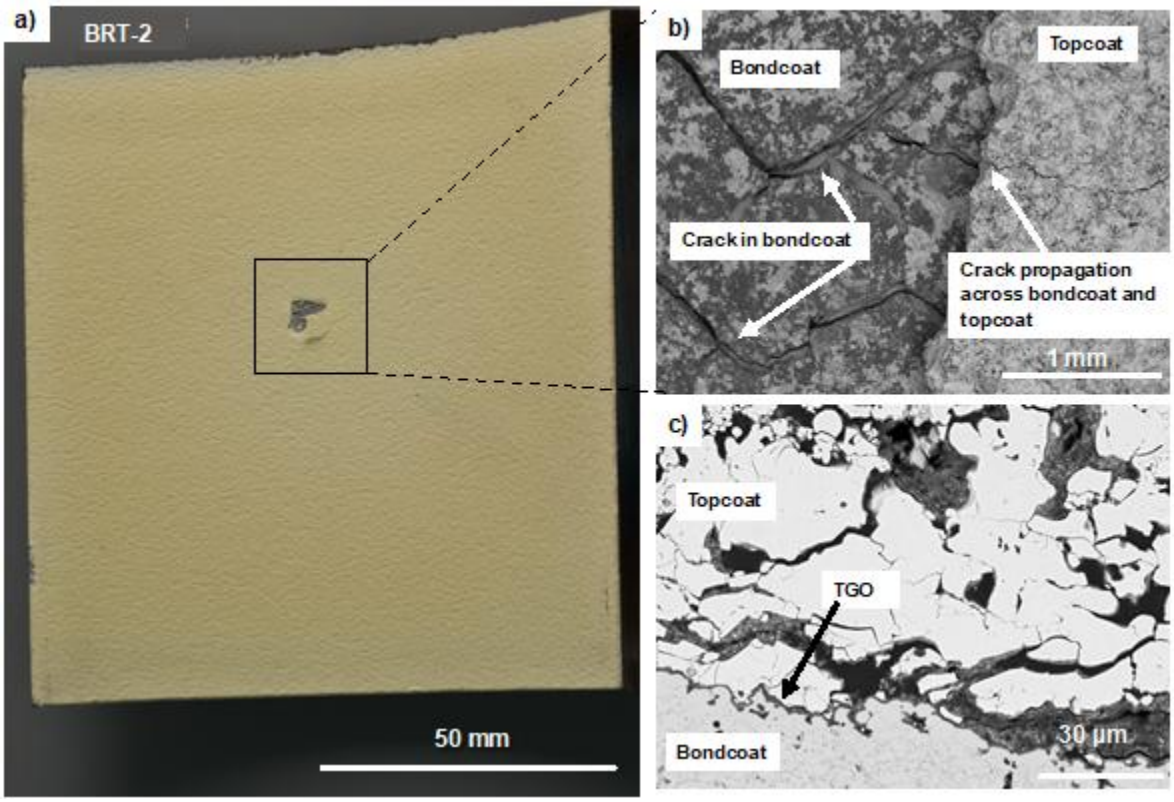

Figure 11. Failure mode of coupon BRT-2 after 101 burner-rig cycles; (a) macroscopic view of the concave flame-side surface; (b) secondary-electron image of the exposed area (inset region in a), showing a through-thickness crack that initiated in the bond-coat and propagated upward into the YSZ top-coat; (c) back-scattered electron cross-section taken beneath the spall: a continuous α-Al_2O_3 TGO (0.5 µm) is present, while a horizontal delamination crack runs immediately above the TGO.

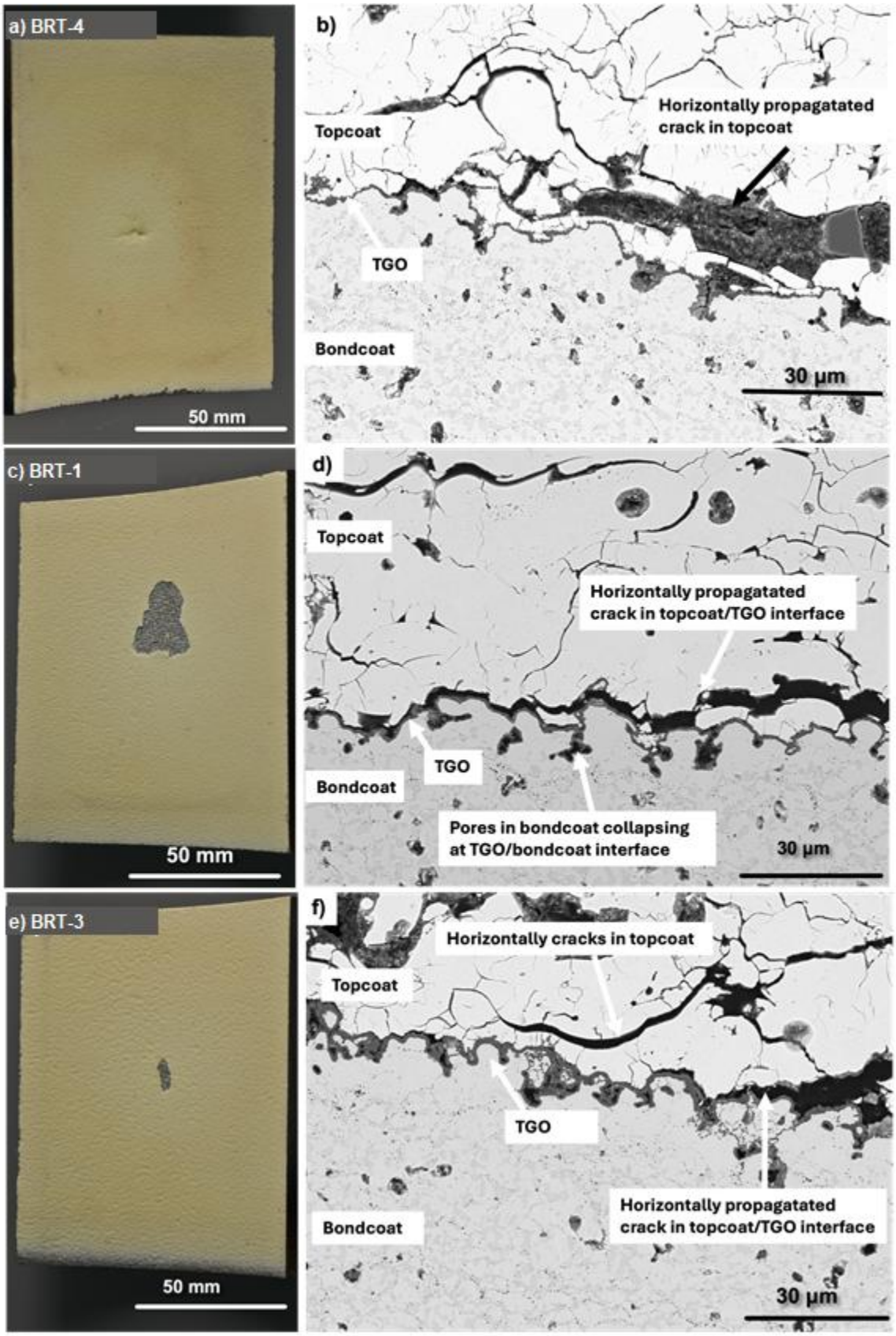

Figure 12. Macroscopic appearance and failure cross-sections of the three ID-TBC samples after burner-rig cycling; (a, b) BRT-4: only a small surface blemish is visible; section (b) reveals a 0.5 µm α-Al_2O_3 TGO and a horizontal crack deflected into the top-coat just above the

interface; (c, d) BRT-1: a single spall patch formed in the middle; section (d) shows a similar delamination crack plus collapsed bond-coat pores at the TGO/metal interface; (e, f) BRT-3: a narrow spall strip is evident; section (f) displays multiple horizontal cracks in the top-coat and along the TGO.

Crucially, the CoNiCrAlY bond coat develops an α-Al_2O_3 scale as its TGO provided there is sufficient aluminum in the coating. α-Alumina grows at a much lower rate than mixed oxides, such as spinel or NiO , so even at a surface temperature of 1320 °C, the TGO growth rate was modest. The Al depletion zones measured in the bond coats (6.8–11.8 µm depth of aluminum consumption beneath the TGO, Table 5) confirm that they were actively supplying aluminum to form alumina and had not exhausted the Al reservoir. The zones were 6.8–11.8 µm deep. In TBC systems, critical aluminum depletion can lead to the formation of transient non-alumina oxides, which dramatically increase the oxidation rate, induce high stress, and often cause spallation [34]. In our tests, the fact that the TGO remained thin and adherent indicates that the coatings never reached the critical depletion point. Given that the bond coat still had aluminum in the first 7–12 µm and the oxide was adherent, the thin TGO was likely pure α-Al_2O_3 with minimal spinel formation.

Bond coat temperature dependence and Arrhenius-type lifetime

According to literature on TBC burner testing, lifetime often correlates with an Arrhenius dependence on bond coat temperature [16, 35]. TGO growth in MCrAlY bond coats is a diffusion-driven, thermally activated process. Table 6 shows the bond-coat temperatures calculated based on the surface and substrate peak temperatures.

In Figure 13 plots the cycle numbers to failure logarithmically against the reciprocal of the bond-coat temperature (1000 K/TBC). According to the Arrhenius approach, data points for samples with comparable lifetime capacities are located close to a straight line, regardless of the testing temperature. Based on experience, increasing the bond coat temperature by 30 K results in halving the lifetime [15, 35]. This is expressed by the slope of the dashed straight line in Figure 13. The samples BRT-2 (1010 °C), BRT-3 (998 °C), and BRT-4 (984 °C) perform similarly because they are close to the line. In contrast, BRT-1 (1045°C) performs significantly better. It survived 163 cycles, which is three times more than the approximate 50 cycles predicted at this temperature by the straight line. BRT-1 is the sample with the highest top coat

porosity. It was sprayed at a higher distance and with lower plasma power. The high porosity of the top coat is assumed to lead to improved compliance, resulting in lower thermal stresses and fewer cracks.

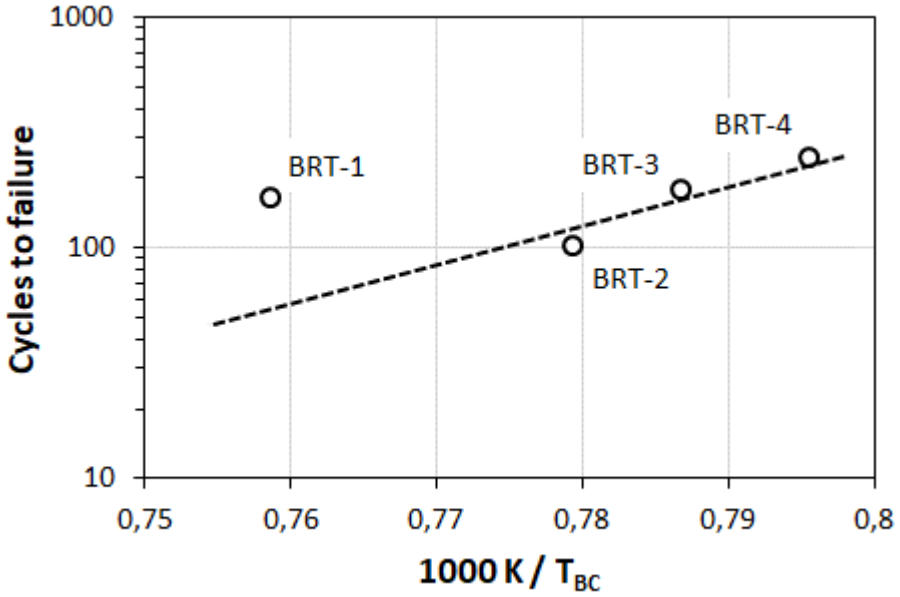

Figure 13. Arrhenius-type life plot for burner-rig specimens; the logarithm of the number of cycles to failure is plotted against the reciprocal bond-coat temperature, 1000 K/T_{BC}.

Bond coat microstructural degradation

Figure 14 shows the microstructural changes in the CoNiCrAlY bond coat of sample BRT-2 before and after 101 thermal cycles. In its as-sprayed state (Figure 14 a), the bond coat is dominated by a continuous NiAl matrix with sparse Kirkendall voids. After burner-rig cycling (Figure 14 b), the Al-rich β-phase becomes visible and the sub-TGO region exhibits significant Al depletion. This evolution demonstrates how early phase transformations can occur, especially when the bond coats are thin.

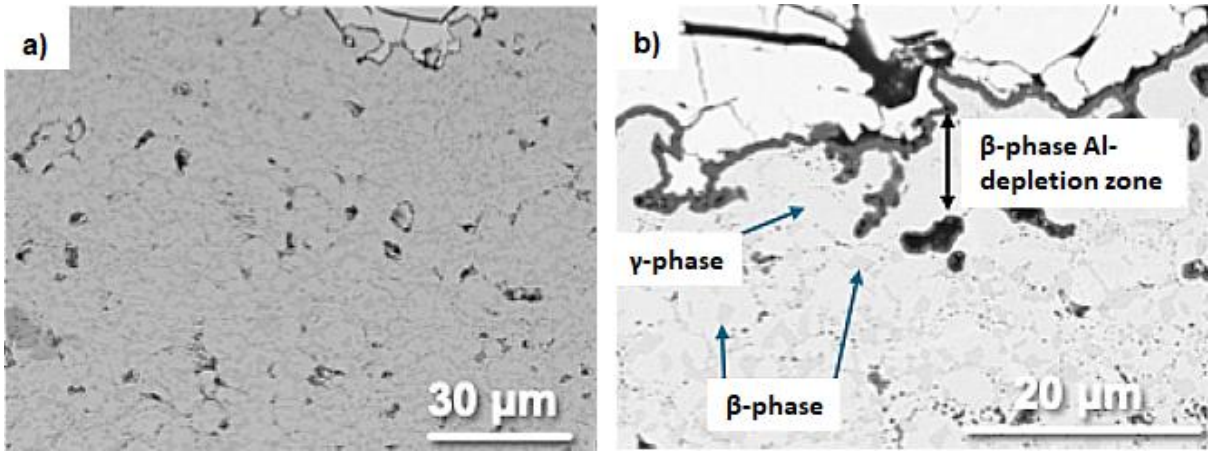

Figure 14. Microstructural evolution of the CoNiCrAlY bond coat in sample BRT-2; (a) a featureless, dark grey matrix with some small pores in as-deposited condition; (b) Al-depleted zone (labelled) immediately under the TGO; the contrast void strings indicate where Al diffused outward to feed the TGO during 101 burner-rig cycles.

Correlation-matrix analysis of design parameters and performance

To quantify the relative influence of three controllable design parameters (top-coat thickness, as-sprayed porosity, and bond-coat thickness) on key performance metrics during burner-rig cycling, Pearson correlation coefficients (r) were computed for each parameter response pair (Table 7). Due to the small sample size (n = 4), only values of $|r| > 0.80$ are considered to be strong, mechanistically meaningful trends.

*Table 7. Correlation matrix (*r*) for ID-TBC burner-rig study, columns list design parameters (topcoat thickness, as-sprayed porosity, and bond coat thickness); rows list response variables measured during cycling (cycles to failure, normalized thermal gradient, and per-cycle ΔT drift), values of $|r| > 0.80$ are highlighted.*

	Bond coat thickness (µm)	Top coat thickness (µm)	As-sprayed topcoat porosity (vol %)
No. of cycles	**+0.83**	**+0.83**	−0.55
Temp. gradient (K µm^{-1})	−0.38	**−0.94**	**+0.96**

ΔT-slope (K cycle^{-1})	**-0.91**	-0.38	-0.02

The matrix (Table 7) shows three dominant linear trends that govern burner-rig durability. First, structural thicknesses positively correlate with lifetime: r = +0.83 for bond coat thickness and r = +0.83 for top coat thickness. This suggests that a larger Al reservoir and a longer heat-flow path jointly delay oxidation-induced embrittlement and lower driving stress. These thicknesses are also linked to other responses. Topcoat thickness is strongly inversely correlated with ΔT/t (r = −0.94), while bond coat thickness shows a strong inverse correlation with per-cycle ΔT drift (r = −0.91). A thicker CoNiCrAlY bond coat layer provides an additional benefit in that it retains β-NiAl and creep ductility for a greater number of cycles. Second, topcoat porosity exhibits dual influence. It is strongly positively correlated with the normalized gradient, ΔT/t (r = +0.96), and shows only a moderate inverse correlation with lifetime (r = −0.55). This indicates that higher porosity steepens the ΔT/t gradient and provides additional strain accommodation.

Collectively, these trends indicate that the lifetime can be extended through architectural changes, such as increasing the YSZ top coat thickness or compliant porosity, or thickening the bond coat, in order to drive the effective gradient below 0.8 K μm^{-1} or maintain a bond coat thickness of at least 130 μm.

Isothermal furnace cycling behavior

Isothermal furnace cycling tests were performed on the four porous thermal barrier coatings on the inner surface of the 321H steel tubes (FCT-1 to 4) as well as on one dense vertical cracked (DVC) sample (FCT-5), see Table 4.

Figure 15 plots the number of furnace cycles to failure against the as-sprayed topcoat porosity for the five 1,100 °C, 2-hour/15-minute isothermal tests. FCT-4 (13% porosity) failed first (after 60 cycles); FCT-1 (17% porosity), FCT-2 (14% porosity), and FCT-3 (9% porosity) failed after 80, 100, and 80 cycles, respectively. Figure 16 shows spallation occurring at or slightly above the TGO layer for all porous coatings. The consistently "complete" spallation observed

is related to homogeneous degradation during isothermal testing without radial or in-plane thermal gradients.

The correlation between service life and porosity is only weak (r^2 = 0.42), which is to be expected in the furnace cycle test, as the samples are heated through completely even with top coats that have different thermal conductivity properties. The slight upward trend can be explained by an increase in the compliance of the coating.

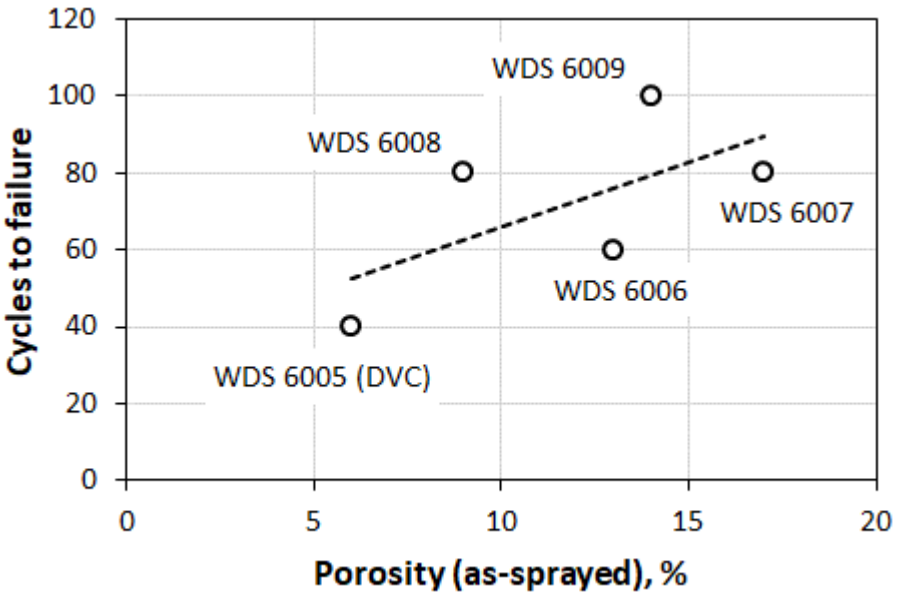

Figure 15. Furnace cycling life time plotted against the as-sprayed top coat porosity.

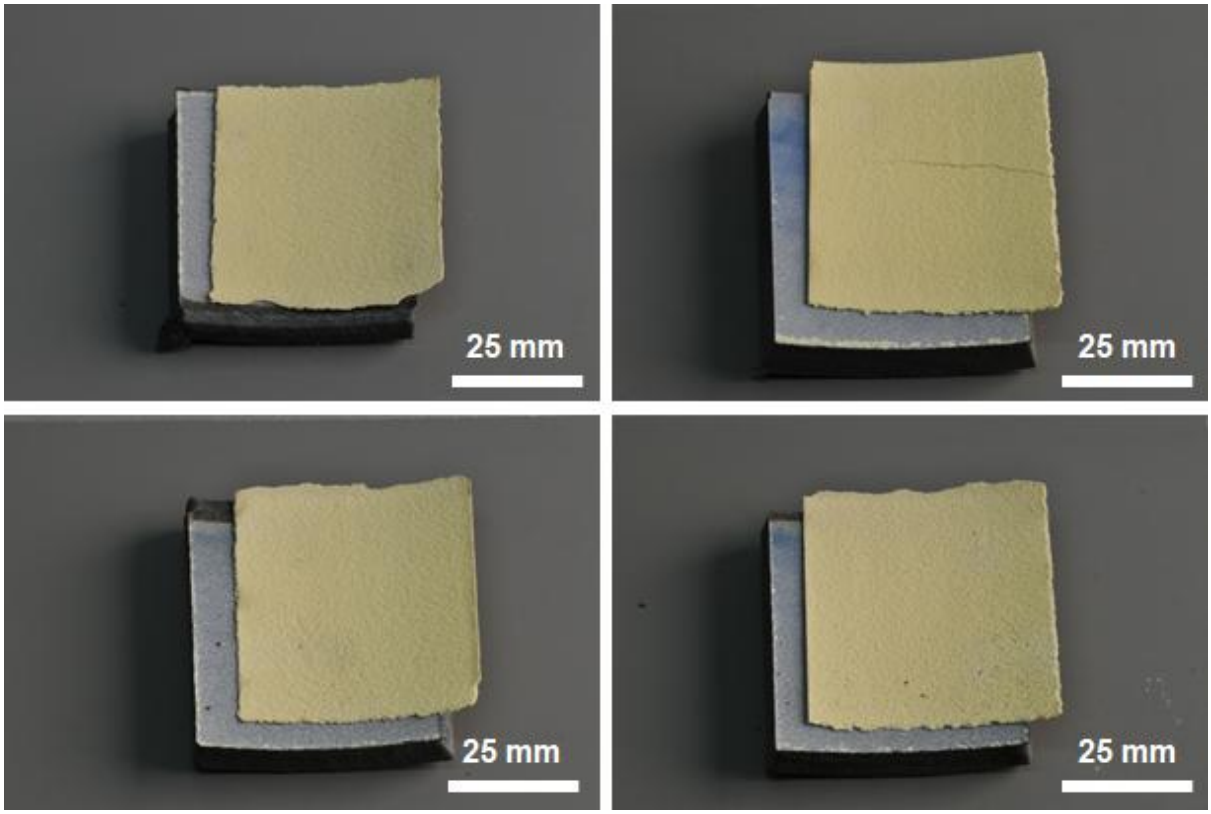

Figure 16. Macroscopic appearance of porous APS coupons after isothermal furnace cycling at 1100 °C; each image shows the coupon immediately after failure; a) FCT-4 after 60 cycles, b) FCT-1 after 80 cycles, c) FCT-3 after 80 cycles, d) FCT-2 after 100 cycles.

The dense-vertical-crack (DVC) reference (FCT-5, 40 cycles) fractured the earliest due to through-thickness cracking in the ceramic topcoat that terminated in the bond coat, though it did not cause complete spallation, as shown in Figure 17. Two cracks spanning the coupons have followed the pre-existing vertical crack network. This indicates that tensile stress in the topcoat, rather than interface delamination, dictated the early failure of this DVC architecture. This underscores the low strain tolerance of a very stiff, low-porosity YSZ topcoat, despite the existing segmentation cracks.

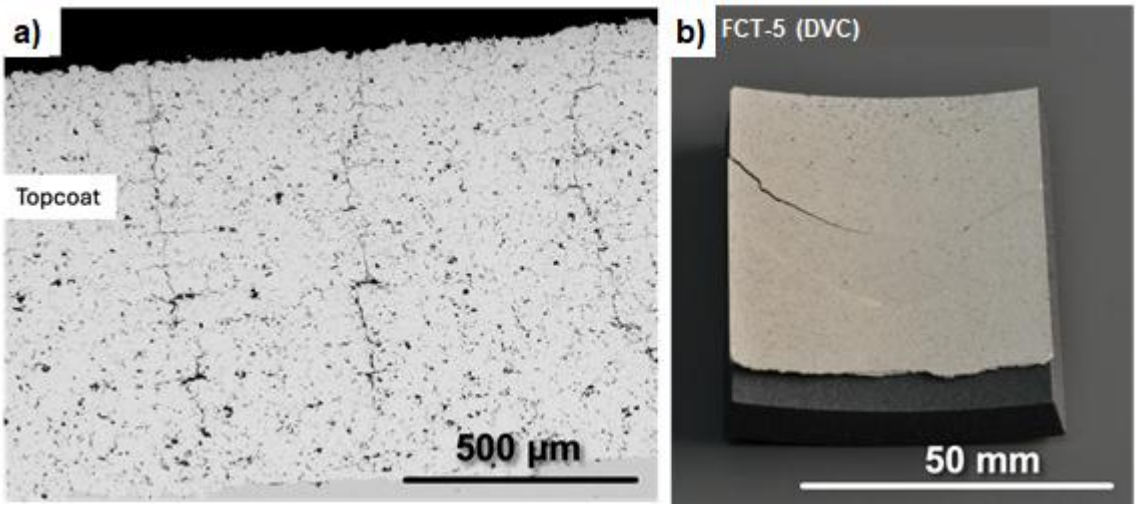

Figure 17. Dense vertical-cracked (DVC) coating FCT-5; (a) as-sprayed SEM cross-section; (b) macroscopic view after 40 furnace cycles.

During each two-hour dwell, all the samples in the isothermal furnace cycles experienced the full 1100 °C at the bond coat/TGO interface. Thus, TGO growth was driven forward with the same intensity for all specimens. Even a porous topcoat could not reduce the bond coat temperature in the static furnace environment, so there is no benefit of a more insulating coating. This explains why absolute lifetimes in furnace cycling (40–100 cycles) were generally lower than in the burner rig for the same coatings.

The stress state after cooling down is harsher in the furnace cycling test than in the burner rig because the thermal gradient causes greater TBC shrinkage. Higher stresses due to fast transient cooling occur more within the ceramic layer, which can cause shallow spallation and segmentation. The burner rig and furnace tests impose different life-limiting factors. The burner rig emphasizes thermal gradient stresses and the need for insulation, favoring porous coatings that keep the bond coat cool. However, toughness and total thickness cannot be neglected. In contrast, the furnace test emphasized high-temperature oxidation.

The lowest number of cycles to failure was 60 for FCT-4 in the furnace cycling test and 101 for BRT-2 in the burner rig test. BRT-4 performed best in the burner rig test with 246 cycles, and FCT-2 performed best in the furnace test with 100 cycles. The worst result in the furnace test occurred at 380 A and 5 slpm H_2, which are high-power conditions. In the burner rig, the worst result was obtained at low power conditions (330 A and 3 slpm H_2). The best results were the exact opposite: the low power conditions were advantageous in the furnace, while the high

power was advantageous in the burner rig. These results confirm the distinct nature of the two tests. A more compliant microstructure performs well in the isothermal furnace test, whereas a highly cohesive microstructure with good adherence to the bond coat and intersplat bonding is advantageous in the burner rig. The best and worst samples were all sprayed at a distance of 70 mm. Samples sprayed at 120 mm performed somewhere in between. These results suggest that plasma power has a greater effect on lifetime than spray distance.

Conclusions

This study examined the collective effect of process parameters, resulting microstructures, and the internal-diameter geometry constraints on the adhesion and thermal cycling durability of ID thermal barrier coatings.

1. The slight difference in porosity observed between curved internal diameter (ID) coatings and flat substrate coatings can be explained by the local splat behavior on curved ID surfaces. The mechanistic basis for the marginally higher porosity of ID substrates compared to flat substrates lies in their single-splat characteristics, altered crack architecture, and increased satellite formation. However, as successive lamellae accumulate, these local variations are averaged out. Ultimately, both flat and tubular substrates develop the same multilayer APS microstructure consisting of an overlapping network of 8YSZ splats with equivalent porosity and intersplat architecture. These findings suggest that substrate curvature, local impact angle, and surface roughness jointly determine initial lamella integrity but do not fundamentally alter the bulk APS coating architecture when process parameters are properly adjusted.
2. Pull-off adhesion testing of ID-APS top coats on ID-HVOF CoNiCrAlY bond coats showed adhesion strengths ranging from 16 to 35 MPa. There was no statistically significant difference between the two stand-off distances of the top coats investigated (70 mm and 120 mm). The consistent fracture location at the bond coat–top coat interface, accompanied by minor glue failure, suggests that adhesion was primarily limited by the ID-HVOF bond coat's relatively low surface roughness, which restricted mechanical interlocking with the ceramic layer. Due to their close similarity in relevant material properties, substituting 316L stainless steel for 321H substrates in the adhesion tests is not expected to have affected these results. These findings underscore the critical role of bond coat surface topography in determining adhesion performance, even when

dense, low-porosity microstructures are achieved. For future ID-HVOF–APS systems, increasing the roughness of the bond coat—either through post-spray surface conditioning or by adjusting deposition parameters to promote higher as-sprayed roughness—appears to be a promising strategy to enhance top coat adhesion.

3. Examinations of metallographic cross sections showed significant variation in BC thickness, even when sprayed at constant parameters. This indicates inconsistencies in the powder feed rate, which result from the considerably lower flowability compared to spray powders in the conventional powder size range. Further research is necessary regarding the addition of flow control agents to enhance the flowability of fine thermal spray powders.
4. Metallographic cross-section examinations revealed that each burner-rig specimen had an adherent α-Al_2O_3 scale approximately 0.5–0.9 μm thick at failure. This scale was underlain by a β-NiAl reservoir several micrometers deep. Since the bond coat had not depleted its aluminum, TGO spallation did not initiate failure. Rather, thermal mismatch stresses resulted in cracks close to the interface, that delaminated the ceramic topcoat while leaving the TGO bonded to the metal.
5. Under burner-rig gradients, durability is controlled by thermo-mechanical load. Coating failure occurs gradually in coatings that maintain a low through-thickness gradient and have a sufficiently thick bond coat. Thinner, hotter coatings, however, delaminate after a single cycle. In isothermal furnace cycling, oxidation dominates. Ultimately, porous APS layers spall off, and the dense DVC architecture cracks first. These results highlight the importance of balanced heat flux, an aluminum reservoir, and strain compliance for achieving long-life ID-TBCs under thermal cycling and isothermal conditions.

Acknowledgements

This work is part of the ID-TBC project, which was funded by the Deutsche Forschungsgemeinschaft (DFG, German Research Foundation) under project number 456827225. The authors would also like to thank the following IMD-2 colleagues at Forschungszentrum Jülich, Germany, for their support: Mr. Karl-Heinz Rauwald and Mr. Frank Kurze assisting with plasma spray coating of the samples, Mr. Martin Tandler for supporting thermal cycling tests, and Mr. Erhan Sucuoglu and the workshop team for helping prepare the tubular substrates.

References

1. Padture, N. P., Gell, M., & Jordan, E. H. (2002). Thermal barrier coatings for gas-turbine engine applications. Science, 296(5566), 280-284.

2. Stöver, D., & Funke, C. (1999). Directions of the development of thermal barrier coatings in energy applications. Journal of Materials Processing Technology, 92, 195-202.

3. Ekström, M., Thibblin, A., Tjernberg, A., Blomqvist, C., & Jonsson, S. (2015). Evaluation of internal thermal barrier coatings for exhaust manifolds. Surface and Coatings Technology, 272, 198-212.

4. Wales, C., Tierney, M., Pavier, M., & Flewitt, P. E. (2019). Reducing steam transport pipe temperatures in power plants. Energy, 183, 127-141.

5. Ernst, P., & Distler, B. (2012). Optimizing the cylinder running surface/piston system of internal combustion engines towards lower emissions (No. 2012-32-0092). SAE Technical Paper.

6. Guo, X., Sun, W., Becker, A., Morris, A., Pavier, M., Flewitt, P., ... & Wales, C. (2019). Thermal and stress analyses of a novel coated steam dual pipe system for use in advanced ultra-supercritical power plant. International Journal of Pressure Vessels and Piping, 176, 103933.

7. Lyphout, C., & Björklund, S. (2015). Internal diameter HVAF spraying for wear and corrosion applications. Journal of Thermal Spray Technology, 24(1), 235-243.

8. Gutleber, J., Molz, R., He, J., Weber, C., & Colmenares, J. (2017, June). New developments in HVOF spraying for internal diameter coatings. In International Thermal Spray Conference (Vol. 83775, pp. 501-504). DVS Media GmbH.

9. Pulsford, J., Venturi, F., Pala, Z., Kamnis, S., & Hussain, T. (2019). Application of HVOF WC-Co-Cr coatings on the internal surface of small cylinders: Effect of internal diameter on the wear resistance. Wear, 432, 202965.

10. Tillmann, W., Schaak, C., Hagen, L., Mauer, G., & Matthäus, G. (2019). Internal diameter coating processes for bond coat (HVOF) and thermal barrier coating (APS) systems. Journal of Thermal Spray Technology, 28(1), 233-241.

11. Baumann, I., Tillmann, W., Schaak, C., Schmidt, K., Hagen, L., Zajaczkowski, J., ... & Luo, W. (2021). internal diameter coating by warm spraying of fine WC-12Co Powders (− 10+ 2 μm) with very short spray distances up to 10 mm. Journal of Thermal Spray Technology, 30(5), 1344-1364.

12. Vaßen, R., Jarligo, M. O., Steinke, T., Mack, D. E., & Stöver, D. (2010). Overview on advanced thermal barrier coatings. Surface and Coatings Technology, 205(4), 938-942.

13. Karger, M., Vaßen, R., & Stöver, D. (2011). Atmospheric plasma sprayed thermal barrier coatings with high segmentation crack densities: Spraying process, microstructure and thermal cycling behavior. Surface and Coatings Technology, 206(1), 16-23.

14. Darolia, R. (2013). Thermal barrier coatings technology: critical review, progress update, remaining challenges and prospects. International materials reviews, 58(6), 315-348.

15. Vaßen, R., Bakan, E., Mack, D. E., & Guillon, O. (2022). A perspective on thermally sprayed thermal barrier coatings: current status and trends. Journal of Thermal Spray Technology, 31(4), 685-698.

16. Igel, J., Scheld, W. S., Mack, D. E., Guillon, O., & Vaßen, R. (2024). Lifetime Extension of Atmospheric and Suspension Plasma-Sprayed Thermal Barrier Coatings in Burner Rig Tests by Pre-Oxidizing the CoNiCrAlY Bond Coats. Coatings, 14(7), 793.

17. Guo, H. B., Vaßen, R., & Stöver, D. (2004). Atmospheric plasma sprayed thick thermal barrier coatings with high segmentation crack density. Surface and Coatings technology, 186(3), 353-363.

18. Shinde, S. V., Johnson, C. A., & Sampath, S. (2020). Segmentation crack formation dynamics during air plasma spraying of zirconia. Acta Materialia, 183, 196-206.

19. Traeger, F., Vaßen, R., Rauwald, K. H., & Stöver, D. (2003). Thermal cycling setup for testing thermal barrier coatings. Advanced Engineering Materials, 5(6), 429-432

20. Li, H., Wang, W., Yang, Z., Liu, Y., Wang, Y., & Liu, W. (2023). Internal Diameter Atmospheric-Plasma-Sprayed High-Performance YSZ-Based Thermal Barrier Coatings. Coatings, 13(11), 1868.

21. Candel, A., Gadow, R., & López, D. (2004). Advanced robot assisted manufacturing and control system for the internal HVOF series coating process of cylinder bores in light weight engine manufacturing. SAE transactions, 232-237.

22. Bagathi, M. R., Vaßen, R., Guillon, O. & Mauer, G. Coating Characteristics of Plasma-Sprayed Ceramic Thermal Barrier Coatings on Internal Diameter (ID) Surfaces. J. Therm. Spray Technol. 34 (2025), 2918-2938

23. Sampath, S., & Jiang, X. (2001). Splat formation and microstructure development during plasma spraying: deposition temperature effects. Materials Science and Engineering: A, 304, 144-150.

24. Chandra, S., & Fauchais, P. (2009). Formation of solid splats during thermal spray deposition. Journal of Thermal Spray Technology, 18(2), 148-180.

25. Tillmann, W., Khalil, O., & Baumann, I. (2021). Influence of direct splat-affecting parameters on the splat-type distribution, porosity, and density of segmentation

cracks in plasma-sprayed YSZ coatings. Journal of Thermal Spray Technology, 30(4), 1015-1027.

26. Mutter, M., Mauer, G., Mücke, R., Guillon, O., & Vaßen, R. (2017). Correlation of splat morphologies with porosity and residual stress in plasma-sprayed YSZ coatings. Surface and Coatings Technology, 318, 157-169.

27. Bursich, S., Morelli, S., Bolelli, G., Cavazzini, G., Rossi, E., Mecca, F. G., ... & Lusvarghi, L. (2024). The effect of ceramic YSZ powder morphology on coating performance for industrial TBCs. Surface and Coatings Technology, 476, 130270.

28. Yalçınyüz, B. A., Kamutzki, F., Gurlo, A., & Rupprecht, C. (2023). Optimization of segmented thermal barrier coatings (s-TBCs) for high-temperature applications. Journal of Thermal Spray Technology, 32(8), 2636-2646.

29. Kang, C. W., & Ng, H. W. (2006). Splat morphology and spreading behavior due to oblique impact of droplets onto substrates in plasma spray coating process. Surface and Coatings Technology, 200(18-19), 5462-5477.

30. Sampath, S., Jiang, X. Y., Matejicek, J., Prchlik, L., Kulkarni, A., & Vaidya, A. (2004). Role of thermal spray processing method on the microstructure, residual stress and properties of coatings: an integrated study for Ni–5 wt.% Al bond coats. Materials Science and Engineering: A, 364(1-2), 216-231.

31. Mahfouz, L., Maurel, V., Guipont, V., Marchand, B., El Hourany, R., Coudon, F., ... & Vaßen, R. (2024). Thermal Barrier Coatings in burner rig experiment analyzed through LAser Shock for DAmage Monitoring (LASDAM) method. Journal of the European Ceramic Society, 44(13), 7867-7882.

32. D'Ans, P., Dille, J., & Degrez, M. (2011). Thermal fatigue resistance of plasma sprayed yttria-stabilised zirconia onto borided hot work tool steel, bonded with a NiCrAlY coating: Experiments and modelling. Surface and Coatings Technology, 205(11), 3378-3386.

33. Li, X., Peng, X. Y., Dong, H., Zhou, Y., Wang, T., Ren, K., & Sun, L. (2019). The evaluation of durability of plasma-sprayed thermal barrier coatings with double-layer bond coat. Coatings, 9(4), 241.

34. Rabiei, A. G. E. A., & Evans, A. G. (2000). Failure mechanisms associated with the thermally grown oxide in plasma-sprayed thermal barrier coatings. Acta materialia, 48(15), 3963-3976.

35. Vorkötter, C., Mack, D. E., Guillon, O., & Vaßen, R. (2019). Superior cyclic life of thermal barrier coatings with advanced bond coats on single-crystal superalloys. Surface and Coatings Technology, 361, 150-158.